



# Monolithically integrated polarization rotator and splitter with designed power ratio

SHUMENG WANG,  PENG LI,  AND JIZE YAN\*

*School of Electronics and Computer Science, University of Southampton, Southampton SO17 1BJ, UK*

*\*J.Yan@soton.ac.uk*

**Abstract:** Inverse designs are widely used for creating ultra-compact photonic devices, but suffer from high computation power due to the optimization complexity. General Stoke's theorem proves that the overall change present at the outer boundary is equal to the integral of the change over the inner intervals, providing the possibility to divide one sophisticated device into several simple building blocks. Thus, we integrate this theorem with the inverse designs as a novel design methodology for optical devices. Compared with conventional inverse designs, the separated regional-optimisations can reduce the computational complexity significantly. The overall computational time is around five times shorter than optimizing the whole device region. To validate the proposed methodology, a monolithically integrated polarization rotator and splitter is designed and fabricated to demonstrate the performance experimentally. The device achieves polarization rotation ( $TE_{00}$  to  $TE_{00}$  and  $TM_{00}$  modes) and power splitting with the designed power ratio. The exhibited average insertion loss is  $<1$  dB and the crosstalk is  $<-9.5$  dB. These findings confirm the advantages of the new design methodology, as well as its feasibility for achieving multiple functions on one monolithic device.

Published by Optica Publishing Group under the terms of the [Creative Commons Attribution 4.0 License](#). Further distribution of this work must maintain attribution to the author(s) and the published article's title, journal citation, and DOI.

## 1. Introduction

Inverse designs have been widely used to design nanophotonic devices [1–4]. The design algorithms allow the users to "design by specification" [5]. Some common algorithms include gradient-based adjoint method [6,7], non-linear direct binary search (DBS) [8,9], genetic algorithm [10,11] and neural network [12]. Compared with conventional designs which strongly depend on physical theory and intuition of researchers [13], the inverse designs can optimize larger parameter space without being over-dependent on physics intuition [14]. These designs allow the realization of ultra-compact photonic devices with sophisticated functionalities [1–25]. The reported devices, such as power splitters [3,4,9,10,12,14], polarization rotators [11,15,21], mode converters [2,22–24], have been realized within a footprint under  $10 \mu m^2$ . [24] achieved multi-functionalities and integrated mode conversion and power splitting into one device using a modified rotatable DBS. However, when two or more functions are integrated into one photonic device, it can be difficult to optimize the design for the whole device, due to slower convergence or being stuck in a "local-maximum" [24]. In addition, the time complexity of DBS grows exponentially with the device scale and can be very time-consuming [25].

To reduce the design complexity, we use General Stoke's theorem to simplify the design space in the inverse designs. This method is widely used in fibre optical systems [26,27], which divides a complicated system into several building blocks with individual functionalities, and then suitable optical components are selected to realise the objectives of the functionalities. The optical components are selected based on physical intuition and understanding of the system architecture. The individual functional component is connected by fibre connectors [28]. We propose to apply similar physical design intuition of the macro-system to the on-chip photonic design, which divides the device into several embedded inverse-designed sub-regions (mini building blocks),

where General Stoke's theorem underlines the physical principle. Each sub-region is optimized by DBS independently to achieve the desired functionality, which will then be used as building blocks to achieve the complete multiple functionalities. Therefore, the whole area-design space optimization is replaced by parallel optimizations of sub-regions, which effectively reduces the optimization complexity and computation time.

To validate our method, we design, fabricate and test a monolithically integrated polarization rotator and splitter with a designed power ratio. The device can fulfil both polarization rotation ( $TE_{00}$  to  $TE_{00}$  and  $TM_{00}$  modes) and power splitting with a designed power ratio. The initial optimization area is separated into three sub-regions; the performance of each sub-region is measured by a figure of merit (FOM), which is optimized using DBS independently. The same constraints are applied to the adjacent boundaries of the sub-regions as design objectives. In this paper,  $TE_{00}:TM_{00}=1:1$ ,  $1:3$  and  $3:1$  are designed and simulated with the largest footprint of  $5.6 \times 2 \mu m^2$ . The device with  $TE_{00}:TM_{00}=1:1$  is fabricated as an experimental demonstration, the measured maximum insertion loss is 1 dB and the crosstalk between  $TE_{00}$  and  $TM_{00}$  modes is less than  $-9.5$  dB. Moreover, the overall computation time for sub-regions optimization is around five times shorter than the whole area optimization via the conventional method. Our method is proven to be an effective method for integrating multi-functionalities into a single photonic device with significantly reduced computational time.

## 2. Design principle

In vector calculus and differential geometry, the Generalized Stoke's theorem discusses the integrations of differential forms on manifolds, which both simplifies and generalizes several theorems from vector calculus. It underlines a design process of breaking down a relatively complex system into a series of simple ones, or a process of merging these simple pieces into the original one. The theorem says that the integral of a differential form over the boundary of some orientable manifold is equal to the integral of its exterior derivative over the whole of the manifold. For example, the 2-D Green's theorem as one special case of the generalized Stoke's theorem defines that the integral of the curl of a vector over the area equals the line integral of this vector around the perimeter. As shown in Fig. 1, the block is cut into small pieces and each has its own circulations. The circulations with reversed directions can cancel each other. Therefore, the circulations from all internal edges cancel out, and on the boundary all the arrows add together to form a giant circulation.

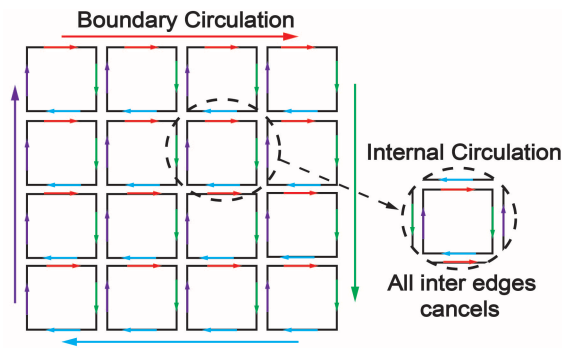


**Fig. 1.** Green's theorem describes the external boundary and internal circulation.

Mathematically, the General Stoke's theorem is given by [29]:

$$\int_{\partial M} \omega = \int_M d\omega. \quad (1)$$

M is the region where a function  $\omega$  is defined and  $\partial M$  is the boundary of this region. Equation (1) indicates that the integral of the derivative of  $\omega$  over M is equal to the integral of  $\omega$  over the boundary of M. Taking the electrostatic field as an example,  $d\omega$  represents the change in electric field of a single charge, which is the divergence. If there is a closed surface  $\partial M$ , the sum of all electric field changes from the charges inside the region M, represented as  $\int_M d\omega$ , is always equal to the total changes on its surface  $\partial M$ , namely the flux. The divergence is a local property, which zooms in and focuses on small changes. While the flux is a global property and describes the changes overall. The General Stoke's theorem governs the relationship between these two properties.

Additionally, assuming that the region M is the superposition of n sub-regions, the right-hand side of Eq. (1) can be rewritten as:

$$\int_M d\omega = \sum_{n=1} \int_{M_n} d\omega_n = \sum_{n=1} \int_{\partial M_n} \omega_n \quad (2)$$

and when combined with the left-hand side, it becomes:

$$\int_{\partial M} \omega = \sum_{n=1} \int_{\partial M_n} \omega_n. \quad (3)$$

According to Eq. (3), all (k+1)-dimensional derivative terms have been replaced by k-dimensional boundary terms, therefore, the boundary condition of a region can induce the internal field functionalities.

The Generalized Stoke's theorem inspires a novel design methodology to design multiple functional photonic devices. In the method, we focus on the design of the external boundaries and the adjacent boundaries between sub-regions. Therefore, the multiple functionalities of a large design region can be split into several single functionalities with smaller sub-design regions. The optimization complexity can be significantly reduced.

Our design method is applied to DBS design. The optimization complexity is significantly reduced. We discrete the design region into m pixels, and assume each pixel has two states "0" and "1"(in this case, "0" refers to silicon while "1" refers to air). Then, the complexity of optimizing this region is defined as  $2^m$ , which exhausts all the possibilities. Now, assuming the region is divided into n sub-regions, the complexity of optimizing each sub-region will be  $2^{\frac{m}{n}}$ . Thereby the total complexity is reduced by  $2^n$  times theoretically, which not only improves the overall optimization efficiency but also avoids the "local-maximum" issue effectively.

However, Eq. (2) has assumed a linear superposition process, which requires that each sub-region is independent of the other. The term "independent" means the original electric field distribution of each sub-region remains unchanged after the merge of sub-regions. This requirement needs further consideration. The change in the local refractive index introduced by the change in the surrounding environment will inevitably impact the original electric field distribution after the merge. This will affect the originally-designed boundary conditions. Thus, additional constraints must be added to the boundaries of adjacent regions to reduce the impact, which will be discussed in the following sections.

### 3. Design of the monolithically integrated polarization rotator and splitter with various power ratios

To validate the proposed method, we design a monolithically integrated polarization rotator and splitter with various power ratios. TE<sub>00</sub> mode is chosen as the input and three different output ratios of TE<sub>00</sub>:TM<sub>00</sub>=1:1, 1:3, 3:1 are numerically demonstrated. Figure 2(a)-(c) are the schematic views of the three designs. The solid lines represent the boundaries connected to the external environment (air), and the dashed lines are the boundaries subjected to the inner

connections. In the design, the whole region is divided into four sub-sections, including the power splitting section, the mode conversion section, the polarization rotation section and the buffering section.

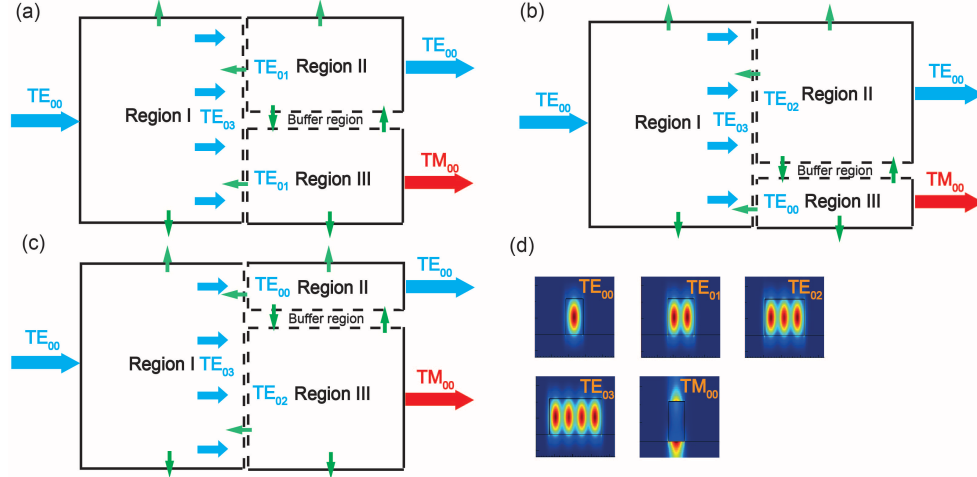


**Fig. 2.** (a)-(c) Schematic views for TE<sub>00</sub>:TM<sub>00</sub>=1:1, TE<sub>00</sub>:TM<sub>00</sub>=3:1 and TE<sub>00</sub>:TM<sub>00</sub>=1:3 respectively. Region I is the power splitting section, Region II is the mode conversion section and Region III is the polarization rotation section. The green arrows represent possible light leakages considered in this paper (d). The cross-section of the ideal input and output modes mentioned in (a) to (c).

For the power splitting section, the Region I. TE<sub>00</sub> mode is injected from the left-side boundary, and the target is to obtain an equally-distributed TE<sub>03</sub> mode on the right-side boundary. To ensure the target mode is equally distributed, the cross-section of the right-side of Region I is equally divided into four parts, and each of which can be regarded as a separate TE<sub>00</sub> mode (as shown in Fig. 2(d)). The FOM in this region is defined as:

$$FOM_I = \alpha \cdot E_{TE_{03}} - (1 - \alpha) \left[ \sum_{n=4} (E_{TE_{00}^n} - 0.25) \right] \quad (4)$$

where  $E$  is the transmittance of mode power. The  $\alpha$  is a parameter used to correct the power ratio of each TE<sub>00</sub> mode under TE<sub>03</sub> mode, making each of them 25 % of the total power. In this way, the total power is expected to be equally allocated to the four TE<sub>00</sub> modes within smaller areas. The different power ratios can be realized by the combined superpositions among these four modes. Light is strongly confined in the core due to the significant refractive index difference between silicon and air, so the losses on the upper and bottom boundaries are assumed to be zero in the simulation.

Mode conversion and polarization rotation are conducted in Region II and Region III, respectively. The equally-distributed TE<sub>00</sub> modes from Region I are the input for Region II and Region III.

For the designed power ratio of TE<sub>00</sub>:TM<sub>00</sub>=1:1, as shown in Fig. 2(a), each small blue arrow represents one equivalent TE<sub>00</sub> separated from TE<sub>03</sub> mode. The input mode of each region is defined to be TE<sub>01</sub>, which is composed of two TE<sub>00</sub> modes in space. The width of each region is designed to be half of the width of Region I so that the upper and lower two TE<sub>00</sub> modes, corresponding to 50 % of the total power, can be confined in the two regions, respectively.

For the designed power ratio of TE<sub>00</sub>:TM<sub>00</sub>=3:1, as shown in Fig. 2(b), the width of Region II and Region III is designed to be three-quarters and one-quarter of the width of Region I,



respectively. The input mode is chosen to be  $TE_{02}$  for Region II and  $TE_{00}$  for Region III, respectively. Similarly, for  $TE_{00}:TM_{00}=1:3$ , we take the same philosophy to divide the boundary, but this time one-quarter of the width of Region I is for Region II. Also the chosen mode for Region II is transferred to  $TE_{00}$ . The process is shown in Fig. 2(c).

For Region II and III, different FOMs are used to evaluate the performance of the final outputs:

$$\text{Region II : } FOM_{II} = E_{TE_{00}} - R_1. \quad (5)$$

$$\text{Region III : } FOM_{III} = E_{TM_{00}} - R_2. \quad (6)$$

The reflections  $R_1$  and  $R_2$  from Region II and Region III to Region I are monitored. The reflections should be minimized to reduce the impact on the output of Region I when the regions are merged. The interaction between Region II and III has not been considered yet, and each region is optimized separately. Light is supposed to be strongly confined in the core region due to the large refractive index difference. The interactions between Region II and Region III will be considered and re-optimized in the buffer region.

After optimizing three regions independently, we merge Region II and Region III, which leads to the merge of adjacent boundaries. The merge results in refractive index change and affects the original light path. To compensate the change, parts of Region II and Region III are re-designated as a buffer region, which will be re-optimized to reduce the impact of the merge. The FOM for buffer region is defined as:

$$FOM_{BR} = E_{TE_{00}} + E_{TM_{00}} - (L_1 + L_2) \quad (7)$$

where  $L_1$  and  $L_2$  monitor the light leakage from Region II and Region III to the buffer region respectively. Only the patterns in the buffer region are re-optimized to improve the  $FOM_{BR}$ . Then, Region I is added to the front end of Region II and III to form a complete device. Here, a buffer region is not needed between Region I and Region II (III). During merging Region I and the rest regions (Region II, Region III and buffer region), the mode power at the end of Region I and the mode powers at the final outputs are monitored. It is found that the mode power at the end of Region I is slightly affected, and the overall mode power loss induced by the merge is less than 5 %. Therefore, no added buffer is utilized in the optimization process.

The DBS method is employed to complete the optimization process [15]. As presented in Fig. 3(a), the proposed structure is optimized by two steps. In step one, three regions are optimized independently to achieve the optimal FOMs mentioned above. For Region I, a manually-set initial pattern is used to avoid local convergence, as the design method is sensitive to the initial patterns [9]. Region II and Region III are optimized, starting from all-silicon. In step two, Region II and Region III are connected by the buffer region. When the optimization of the buffer region is completed, all regions are merged to form the final device, as shown in Fig. 3(b).

The model of  $TE_{00}:TM_{00}=1:1$  is shown in Fig. 3(b). The device is based on an SOI platform with a 220 nm-thick top silicon layer. The widths of the input and output waveguides are 600 nm, and the gap between the two output waveguides are designed to be  $1.2 \mu m$  to avoid crosstalk. The footprint of the design region is  $4.8 \times 2 \mu m^2$ , which is discretized into  $100 \text{ nm} \times 100 \text{ nm}$  pixels. Each pixel has two states: "0" represents silicon, and "1" represents air. The etching depth of the pixel is 220 nm. The design space of Region I is  $2.4 \times 2 \mu m^2$ , which composes of  $24 \times 20$  pixels. For Regions II and III, the widths will fluctuate depending on the corresponding  $TE_{00}:TM_{00}$  power ratio. And the lengths can be increased if larger design space is needed. The bigger the difference in effective index between the input and output in Region II(III) is, the larger design space is required. The length for  $TE_{00}:TM_{00}=1:3$  and  $TE_{00}:TM_{00}=3:1$  is set to be  $3.2 \mu m$  to increase the design space. The overall number of pixels is  $32 \times 20$ .

The 3D finite-difference time-domain (FDTD) method is utilized to calculate the FOM using Lumerical FDTD Solutions. The simulations finish when the FOM growth falls below 1%. The

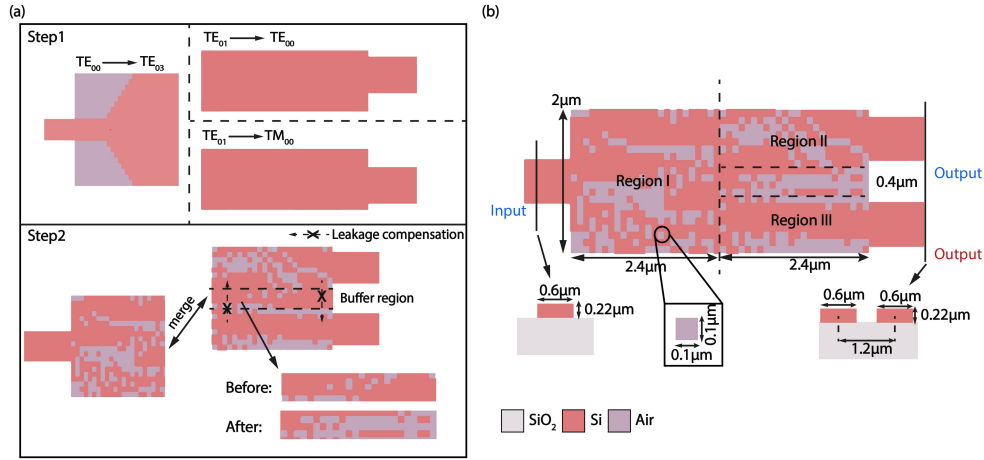


**Fig. 3.** (a) The simulation steps for the proposed device. (b) Optimized structure of TE<sub>00</sub>:TM<sub>00</sub>=1:1.

overall optimization time for TE<sub>00</sub>:TM<sub>00</sub>=1:1 is 17 hours, and it takes a bit longer for the other two ratios, which are within 20 hours. The optimizations are operated on the IRIDIS High Performance Computer Cluster.

## 4. Results and discussion

### 4.1. Performance evaluation

Figure 4 illustrates the  $E_y$  and  $E_z$  electric field profiles and the transmission spectra for TE<sub>00</sub>:TM<sub>00</sub>=1:1, 1:3 and 3:1, respectively. The initial TE<sub>00</sub> is gradually evolved into our expected modes with a specific power ratio based on the merged regions. For TE<sub>00</sub>:TM<sub>00</sub>=1:3 (Fig. 4(d) and (e)), Region II only has TE<sub>00</sub> mode transmission, and no mode conversion is happened.

To evaluate the accuracy of the designed power ratio, we define the actual power ratio minus the ideal power ratio as the power ratio error (PRE) [10], as summarised in Table 1. The PRE for TE<sub>00</sub>:TM<sub>00</sub>=1:1 is less than 0.12, and continuously decreases as the wavelength increases from 1500 nm and reduces to zero at 1590 nm. The overall transmission efficiency is above 85% over the wavelength range of 1500 nm-1600 nm.

**Table 1. PRE of the three design ratios.**

Power ratio error (PRE)			
TE:TM Power ratio	1:1	1:3	3:1
Maximum PRE	0.12	0.16	0.16

For both TE<sub>00</sub>:TM<sub>00</sub>=1:3 and TE<sub>00</sub>:TM<sub>00</sub>=3:1, the PRE is less than 0.16. For TE<sub>00</sub>:TM<sub>00</sub>=1:3, the peak of PRE appears within the wavelength of 1500 nm-1550 nm due to the descending transmission for TE<sub>00</sub>. For TE<sub>00</sub>:TM<sub>00</sub>=3:1, the peak of PRE appears within 1550 nm-1600nm. The transmission of TE<sub>00</sub> within 1550 nm-1600 nm is lower than that within 1500 nm-1550 nm, but the transmission of TM<sub>00</sub> is relatively stable within the whole bandwidth. The overall PRE increases within 1550 nm-1600nm.

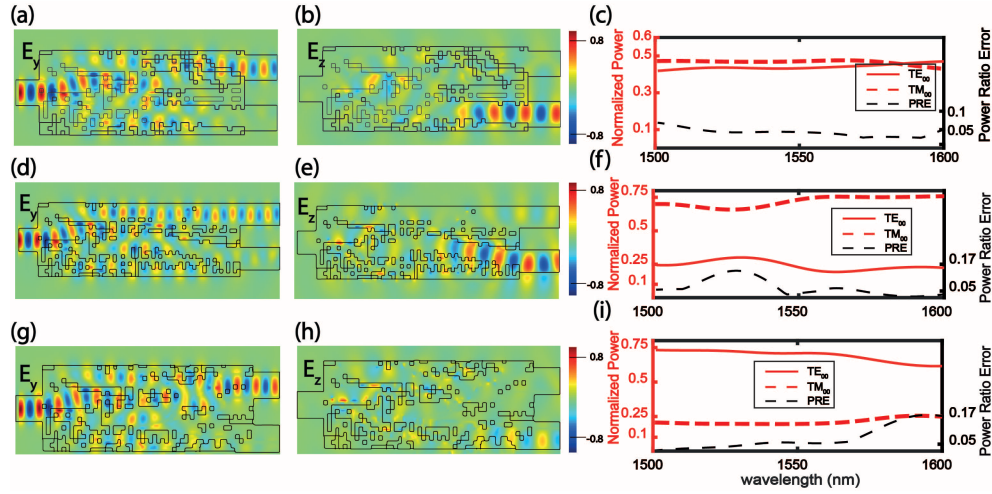


**Fig. 4.** The calculated  $E_y$  and  $E_z$  electric field profiles at 1500 nm and transmission spectra under the wavelength range from 1500 nm-1600 nm for (a)-(c)  $TE_{00}:TM_{00}=1:1$ , (d)-(f)  $TE_{00}:TM_{00}=1:3$  and (g)-(i)  $TE_{00}:TM_{00}=3:1$ .

#### 4.2. Effect of the buffer region on merging Region II and Region III

In addition, we also investigate the effects of the buffer region. The region width is initially chosen to be  $0.4 \mu\text{m}$  to balance design space and simulation time. As shown in Fig. 3(a), most of the buffer region is removed after the optimization because the buffer region is optimized to isolate Region II and Region III towards the extreme case of being physically separated. Also, most of the upper edge of Region III is removed, the buffer region modifies the bottom edge of Region II so that they can be isolated from each other. It found that buffer region improves the overall transmission by eliminating other higher-order modes introduced by merging Region II and Region III. Figure 5(a) and (b) illustrate the normalized output transmissions and crosstalks of  $TE_{00}:TM_{00}=1:1$  before and after the buffer region is added. The crosstalk represents the difference between the target mode and the summation of other unwanted modes. The insertion loss is reduced by  $\sim 0.8 \text{ dB}$  for  $TE_{00}$  and  $TM_{00}$  modes. This is realized through physical isolation and converting other high-order modes to the target modes, where the crosstalk is decreased by at least 5 dB.

The buffer region also plays a vital role similar to the other designed power ratios. Its effect on the mode purity is as shown in Fig. 5(c)-(f): The minimum crosstalk is decreased by 5 dB and 10 dB for  $TE_{00}:TM_{00}=1:3$  and  $TE_{00}:TM_{00}=3:1$ , respectively. The merge of Region II and Region III has a relatively more significant impact on Region III. The refractive index of  $TM_{00}$  mode is relatively small and easier to be converted from other modes.

#### 4.3. Impact of merging Region II and Region III into Region I

Despite contributions that have been made to the FOMs when optimizing Region II (III) to decrease the reflections from these regions to Region I, the output  $TE_{03}$  mode is still inevitably affected. A wide region of  $\alpha$  is scanned for the  $FOM_I$  during the optimization of Region I to ensure that the maximum transmission of  $TE_{03}$  is obtained and each "small"  $TE_{00}$  is equally distributed. Ideally, the four  $TE_{00}$  modes are expected to be equally distributed within  $0.5 \mu\text{m}$  width, and each one has 25% of the total net power. As indicated by the red line in Fig. 6(a), each spike represents one separate  $TE_{00}$  mode.

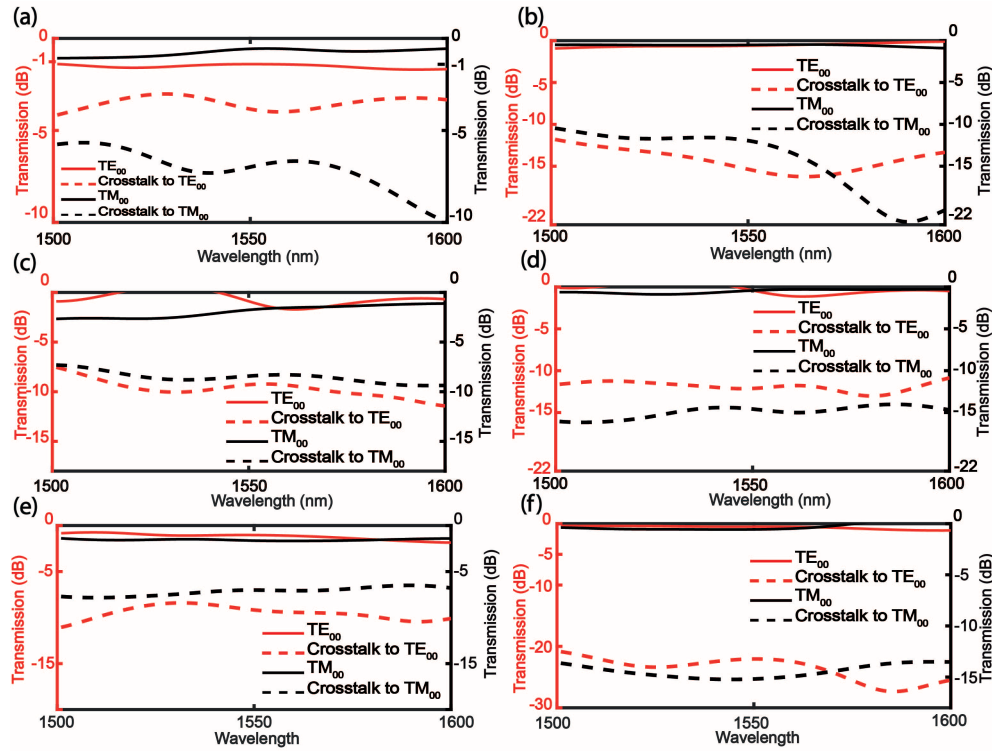


**Fig. 5.** The normalized transmission spectra before and after adding the buffer region. (a)-(b)  $TE_{00}:TM_{00}=1:1$ . (c)-(d)  $TE_{00}:TM_{00}=1:3$ . (e)-(f)  $TE_{00}:TM_{00}=3:1$ .

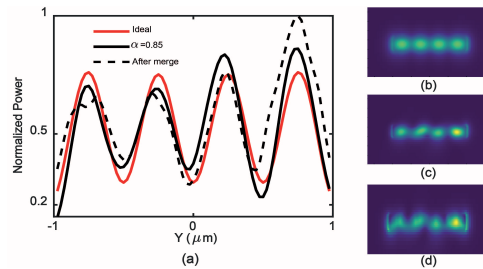


**Fig. 6.** (a) The comparisons of normalized power distributions of the cross section at the end of Region I between the ideal, optimized and merged situations. (b)-(d) the corresponding electric field profiles of the cross sections.

The results of different  $\alpha$  from 0.5 to 0.9 are analyzed: It is found that the electric field distribution at  $\alpha = 0.85$ , represented by the solid black line in Fig. 6(a), shows the highest consistency with the ideal result. Electric field profiles of the ideal result and  $\alpha = 0.85$  are shown in Fig. 6(b) and (c), respectively. The optimized transmission for  $TE_{03}$  is 92%, and the amplitude error of each separated  $TE_{00}$  mode is less than 5%. The black dashed line in Fig. 6(a) is the result after Region II and III are added. It shows that the highest amplitude of power of the 4th  $TE_{00}$  mode is increased by 5% from the ideal one. This inconsistency will affect the total power distribution and increase power ratio error for  $TE_{00}$  and  $TM_{00}$  at the outputs. The cross-section shown in Fig. 6(d) indicates that the original elliptical light spots have been slightly deformed,

especially for the first and second  $TE_{00}$  modes. The widths of these modes are also increased. The overall transmission decreases  $\sim 6\%$  after Region I is added.

#### 4.4. Improved computational time and device performance

For comparison, a reference model of  $TE_{00}:TM_{00}=1:1$  without region separation was optimized in the same design space using the normal DBS method, shown in Fig. 7(b). The FOM of the reference device is defined as the summation of total power under  $TE_{00}$  and  $TM_{00}$  from the upper and lower output, respectively. Figure 7(a) shows the calculated FOMs of models with and without region separation, the simulation results are summarized in Table 2.

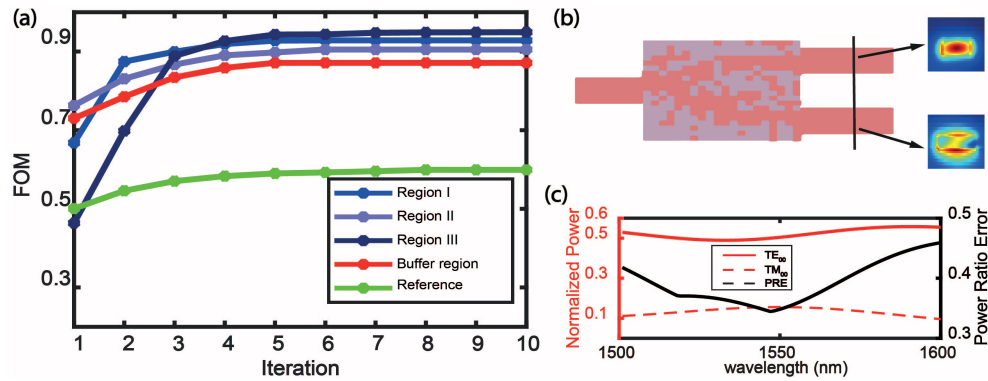


**Fig. 7.** (a) The calculated FOMs of the proposed and reference models of  $TE_{00}:TM_{00}=1:1$ . The optimization time for Region I, Region II and Region III are 16 hours, 9 hours and 9 hours respectively. The re-optimization of the buffer region took 8 hours for 5 iterations. For the reference device, as the optimization space enlarges, it took 16 hours for only 1 iteration. (b) and (c) The optimized reference model and its transmission spectra. The inserts are the generated  $TE_{00}$  and  $TM_{00}$  modes, where  $TM_{00}$  is affected by high-order modes.

**Table 2. The comparison between the proposed and reference models of  $TE_{00}:TM_{00}=1:1$ .**

Region	Proposed device				Reference device
	I	II	III	Buffer region	
# Iterations before stabilization	5	6	5	5	8
Maximum FOM	0.92	0.91	0.93	0.87	0.59
Time cost (h)	16	9	9	8	80

It takes 9 hours to optimize Region II and Region III. The optimization of the buffer region takes 8 hours for 5 iterations. The optimization of Region I takes 16 hours for the pattern to be generated. Using the parallel optimization method, the overall computational time is 17 hours.

The FOMs for the proposed device are above 0.85 after 5 to 6 iterations. The final FOMs for Region II and Region III are 0.91 and 0.93, corresponding to over 90 % of  $TE_{00}$  and  $TM_{00}$  mode power respectively. When two regions are merged without the buffer region, the overall transmissions for both modes decrease. The  $FOM_{BR}$  are by the red line in Fig. 7(a). The initial  $FOM_{BR}$  of the buffer region is 0.72, it corresponds to  $\sim 72\%$  of total power, which is  $\sim 20\%$  lower than the output before merging. During the optimization of the buffer region, we monitor the mode powers ( $TE_{00}$  and  $TM_{00}$ ) at the outputs. After five iterations, the mode powers for both modes increase  $\sim 15\%$ , and the corresponding  $FOM_{BR}$  raises from 0.72 to 0.87 and then stabilizes.



For the reference device, as shown by the green line in Fig. 7, the maximum FOM is 0.59. The corresponding  $TE_{00}$  and  $TM_{00}$  power are 48 % and 10 % respectively. The maximum PRE is 0.43, and most of its contribution comes from the error of  $TM_{00}$  mode. In contrast, the overall transmission of the reference device is 33% lower than the proposed one. Moreover, because there is no regional separation, the optimization process cannot be carried out independently. The iteration will require a much longer computational time. E.g. The recorded time for five iterations of the reference device is 80 hours.

## 5. Experimental verification

To evaluate our method, the device with  $TE_{00}:TM_{00}=1:1$  is fabricated based on a SOI wafer with a 220-nm Si layer and 3- $\mu\text{m}$  buried oxide layer. The wafer is firstly coated by 300-nm ZEP520A photoresist with spacer using resist spinner. Then, electron-beam lithography is used to form the pattern of the waveguide. After that, spacer is removed by DI water and the photoresist is developed using ZED-N50 developer. The inductively coupled plasma etching is then utilized to etch a depth of 220 nm. Finally, ellipsometry is performed to confirm the etching depth after etching. We also fabricate TE-type and TM-type grating couplers for coupling the target modes into or out of optical fibers. The etching depth for both types of grating couplers are 70 nm, and the fabrication process is the same as we mentioned above. Figure 8(c)- (e) are the zoomed-in SEM images of the grating couplers and the device, respectively. To make sure  $TE_{00}$  mode is converted to  $TM_{00}$  mode, a reference device as shown in Fig. 8(a) is designed, the output  $TE_{00}$  and  $TM_{00}$  are coupled out by only TM-type grating couplers. The result is shown in Fig. 8(f), where the measured average transmissions for  $TE_{00}$  and  $TM_{00}$  modes are around -12dB and -3.5dB within the range of 1540nm to 1560nm, respectively. The smallest value for  $TE_{00}$  mode

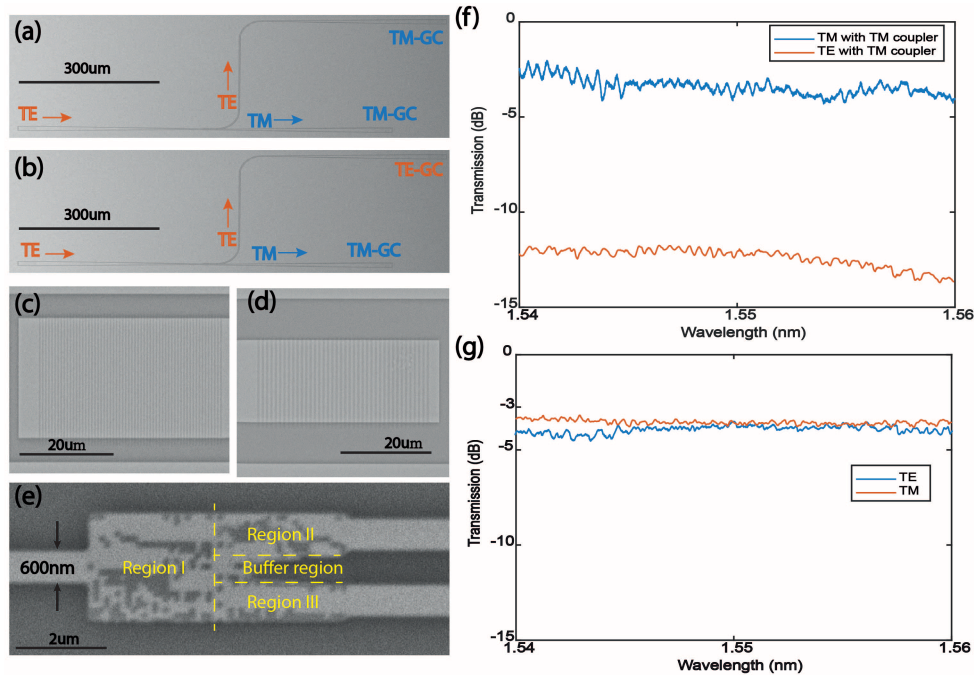


**Fig. 8.** SEM of a TE:TM=1:1 device with (a) TE-input and two TM-outputs. (b) TE-input and upper-TE-output, bottom-TM-output. (c) and (d) The zoomed in SEM image of TE and TM grating couplers. (e) The zoomed in SEM image of the device. The experimental spectra for (f) TE-input and two TM-outputs, (g) TE-input and upper-TE-output, bottom-TM-output.



is  $-14$  dB at  $1560$  nm, the average crosstalk is therefore below  $-9.5$  dB when comparing the two modes. After confirming the effectiveness of  $TE_{00}$ - $TM_{00}$  conversion, the device is then measured by TE-type and TM-type grating couplers shown in Fig. 8(b). The result is shown in Fig. 8(g). For  $TM_{00}$  mode, the average insertion loss is  $0.6$  dB, the maximum value is around  $0.7$  dB at  $1550$  nm. For  $TE_{00}$  mode, the insertion loss is a bit higher within the region of  $1540$  nm to  $1546$  nm, which is around  $1$  dB, the minimum insertion loss is  $0.7$  dB at  $1550$  nm. Overall, the measured data are in good agreement with the simulated results, which validates the feasibility of our method experimentally.

## 6. Conclusion

In conclusion, we combine the General Stoke's theorem and DBS to propose a novel design methodology. Based on the proposed method, the whole design region is separated into several sub-regions, which can be optimized simultaneously. The simulation complexity can be reduced by  $2^n$  times theoretically. When sub-regions are merged, additional constraints are added to the adjacent boundaries to reduce the impact of the merge. Finally, sub-regions are merged to achieve the functionality of the whole device. As a validation, monolithically integrated polarization rotators and splitters with various power ratios are numerically designed. Device with  $TE_{00}:TM_{00}=1:1$  is fabricated in our cleanroom to validate the design method, the measured results show that the maximum insertion loss is  $1$  dB ( $TE_{00}$  mode from  $1540$  nm to  $1546$  nm), and the average crosstalk is below  $-9.5$  dB. There are two potential ways to further improve the crosstalk. Firstly, the size of each sub-region can be further enlarged to increase the design space. Secondly, the pixels can be partially etched instead of fully etched to increase the mode conversion efficiency. There is a trade-off between the two potential ways, as large size requires longer optimization time and multiple etching steps bring extra fabrication complexity compared with a single etching step.

Different power ratios can be realized by changing the output mode of Region I and different combined superpositions of input modes of Region II and Region III, respectively. As the simulation complexity is decreased, the overall simulation time is  $17$  hours, which is around five times faster than the reference device. We envisage that our device will have more applications in on-chip pumping and probing system [30] and the generation of arbitrary first-order Poincaré sphere beams [31]. As long as sub-regions are carefully designed so that their boundaries are matched, our proposed method will give a solution for designing other multi-functional photonic devices.

**Funding.** Engineering and Physical Sciences Research Council (EPSRC EP/V000624/1).

**Acknowledgments.** The authors acknowledge the use of the IRIDIS High Performance Computing Facility at the University of Southampton in the completion of this work. The authors also acknowledge Mr. Chuang Sun for his useful feedbacks on this manuscript.

**Disclosures.** The authors declare no conflicts of interest

**Data availability.** The data that support the findings of this study are openly available at the University of Southampton ePrints research repository [32].

## References

1. Y. Meng, Y. Chen, L. Lu, Y. Ding, A. Cusano, J. A. Fan, Q. Hu, K. Wang, Z. Xie, and Z. Liu, "Optical meta-waveguides for integrated photonics and beyond," *Light: Sci. Appl.* **10**(1), 235 (2021).
2. M. Teng, K. Kojima, T. Koike-Akino, B. Wang, C. Lin, and K. Parsons, "Broadband SOI mode order converter based on topology optimization," in *2018 Optical Fiber Communications Conference and Exposition (OFC)*, (IEEE, 2018), pp. 1–3.
3. H. Xie, Y. Liu, W. Sun, Y. Wang, K. Xu, J. Du, Z. He, and Q. Song, "Inversely designed  $1 \times 4$  power splitter with arbitrary ratios at  $2\text{-}\mu\text{m}$  spectral band," *IEEE Photonics J.* **10**(4), 1–6 (2018).
4. K. Goudarzi, D. Kim, H. Lee, I. Park, and H. Han, "Ultra low loss broadband  $1 \times 2$  optical power splitters with various splitting ratios," *Opt. Continuum* **1**(9), 1888–1895 (2022).

5. A. Y. Piggott, J. Lu, K. G. Lagoudakis, J. Petykiewicz, T. M. Babinec, and J. Vučković, "Inverse design and demonstration of a compact and broadband on-chip wavelength demultiplexer," *Nat. Photonics* **9**(6), 374–377 (2015).
6. J. S. Jensen and O. Sigmund, "Topology optimization for nano-photonics," *Laser Photonics Rev.* **5**(2), 308–321 (2011).
7. C. M. Lalau-Keraly, S. Bhargava, O. D. Miller, and E. Yablonovitch, "Adjoint shape optimization applied to electromagnetic design," *Opt. Express* **21**(18), 21693–21701 (2013).
8. Y. Liu, H. Li, W. Chen, P. Wang, S. Dai, B. Zhang, J. Li, Y. Li, Q. Fu, and T. Dai, "Direct-binary-search-optimized compact silicon-based polarization beam splitter using a pixelated directional coupler," *Opt. Commun.* **484**, 126670 (2021).
9. H. Ma, J. Huang, K. Zhang, and J. Yang, "Arbitrary-direction, multichannel and ultra-compact power splitters by inverse design method," *Opt. Commun.* **462**, 125329 (2020).
10. Y. Xie, T. Huang, Q. Ji, M. Yang, J. Wang, X. Tu, Z. Cheng, G. Xu, Q. Wei, and Y. Wu, "Design of an arbitrary ratio optical power splitter based on a discrete differential multiobjective evolutionary algorithm," *Appl. Opt.* **59**(6), 1780–1785 (2020).
11. Z. Yu, H. Cui, and X. Sun, "Genetic-algorithm-optimized wideband on-chip polarization rotator with an ultrasmall footprint," *Opt. Lett.* **42**(16), 3093–3096 (2017).
12. M. H. Tahersima, K. Kojima, T. Koike-Akino, D. Jha, B. Wang, C. Lin, and K. Parsons, "Deep neural network inverse design of integrated photonic power splitters," *Sci. Rep.* **9**(1), 1368 (2019).
13. R. Halir, P. Cheben, J. M. Luque-González, J. D. Sarmiento-Merenguel, J. H. Schmid, G. Wangüemert-Pérez, D.-X. Xu, S. Wang, A. Ortega-Monux, and Í. Molina-Fernández, "Ultra-broadband nanophotonic beamsplitter using an anisotropic sub-wavelength metamaterial," *Laser Photonics Rev.* **10**(6), 1039–1046 (2016).
14. H. Ma, J. Huang, K. Zhang, and J. Yang, "Inverse-designed arbitrary-input and ultra-compact  $1 \times N$  power splitters based on high symmetric structure," *Sci. Rep.* **10**(1), 1–7 (2020).
15. A. Majumder, B. Shen, R. Polson, and R. Menon, "Ultra-compact polarization rotation in integrated silicon photonics using digital metamaterials," *Opt. Express* **25**(17), 19721–19731 (2017).
16. D. Dai and J. E. Bowers, "Novel concept for ultracompact polarization splitter-rotator based on silicon nanowires," *Opt. Express* **19**(11), 10940–10949 (2011).
17. Y. Liu, S. Wang, Y. Wang, W. Liu, H. Xie, Y. Yao, Q. Song, X. Zhang, Y. Yu, and K. Xu, "Subwavelength polarization splitter-rotator with ultra-compact footprint," *Opt. Lett.* **44**(18), 4495–4498 (2019).
18. J. Huang, J. Yang, D. Chen, X. He, Y. Han, J. Zhang, and Z. Zhang, "Ultra-compact broadband polarization beam splitter with strong expansibility," *Photonics Res.* **6**(6), 574–578 (2018).
19. L. H. Frandsen and O. Sigmund, "Inverse design engineering of all-silicon polarization beam splitters," in *Photonic and Phononic Properties of Engineered Nanostructures VI*, vol. 9756 (SPIE, 2016), pp. 48–53.
20. B. Shen, P. Wang, R. Polson, and R. Menon, "An integrated-nanophotonics polarization beamsplitter with  $2.4 \times 2.4 \mu\text{m}^2$  footprint," *Nat. Photonics* **9**(6), 378–382 (2015).
21. W. Chang, S. Xu, M. Cheng, D. Liu, and M. Zhang, "Inverse design of a single-step-etched ultracompact silicon polarization rotator," *Opt. Express* **28**(19), 28343–28351 (2020).
22. T. Wang, H. Guo, H. Chen, J. Yang, and H. Jia, "Ultra-compact reflective mode converter based on a silicon subwavelength structure," *Appl. Opt.* **59**(9), 2754–2758 (2020).
23. H. Jia, H. Chen, J. Yang, H. Xiao, W. Chen, and Y. Tian, "Ultra-compact dual-polarization silicon mode-order converter," *Opt. Lett.* **44**(17), 4179–4182 (2019).
24. H. Ma, J. Huang, K. Zhang, and J. Yang, "Ultra-compact and efficient  $1 \times 2$  mode converters based on rotatable direct-binary-search algorithm," *Opt. Express* **28**(11), 17010–17019 (2020).
25. W. Kuang, L. Ma, and Z. He, *et al.*, "Ultra-compact low loss polymer wavelength (de) multiplexer with spot-size converter using topology optimization," *IEEE Photonics J.* **13**(3), 1–9 (2021).
26. J. Song, W. Li, P. Lu, Y. Xu, L. Chen, and X. Bao, "Long-range high spatial resolution distributed temperature and strain sensing based on optical frequency-domain reflectometry," *IEEE Photonics J.* **6**(3), 1–8 (2014).
27. Y. Du, T. Liu, Z. Ding, Q. Han, K. Liu, J. Jiang, Q. Chen, and B. Feng, "Cryogenic temperature measurement using rayleigh backscattering spectra shift by OFDR," *IEEE Photonics Technol. Lett.* **26**(11), 1150–1153 (2014).
28. P. Lu, N. Lalam, M. Badar, B. Liu, B. T. Chorpining, M. P. Buric, and P. R. Ohodnicki, "Distributed optical fiber sensing: Review and perspective," *Appl. Phys. Rev.* **6**(4), 041302 (2019).
29. V. J. Katz, "The history of Stokes' theorem," *Math. Mag.* **52**(3), 146–156 (1979).
30. V. R. Almeida and M. Lipson, "Optical bistability on a silicon chip," *Opt. Lett.* **29**(20), 2387–2389 (2004).
31. H. Pi, W. Yu, J. Yan, and X. Fang, "Coherent generation of arbitrary first-order poincaré sphere beams on an Si chip," *Opt. Express* **30**(5), 7342–7355 (2022).
32. S. Wang, "Dataset for the paper 'A novel method to design the monolithically integrated polarization rotator and splitter with arbitrary power ratio'," University of Southampton (2023) <https://doi.org/10.5258/SOTON/D2323>.